Journal of The Electrochemical Society, **160** (10) A1701-A1710 (2013)
0013-4651/2013/160(10)/A1701/10/$31.00 © The Electrochemical Society

A Comprehensive Capacity Fade Model and Analysis for Li-Ion Batteries

Xianke Lin,[a] Jonghyun Park,[a] Lin Liu,[a] Yoonkoo Lee,[a] A. M. Sastry,[b] and Wei Lu[a,z]

[a]*Department of Mechanical Engineering, University of Michigan, Ann Arbor, Michigan 48109, USA*
[b]*Sakti3, Ann Arbor, Michigan 48108, USA*

A physics-based side-reaction coupled electrochemical model for capacity fade of a graphite/$LiMn_2O_4$ cell is developed by including the key degradation mechanisms in both anode and cathode. The side reactions considered in this study include 1) solid electrolyte interphase (SEI) growth and manganese deposition on the anode and 2) manganese dissolution, electrolyte oxidation and salt decomposition on the cathode. Our study reveals three stages of capacity fade upon long term cycling: acceleration, stabilization, and saturation. In the acceleration stage, capacity fade is due mainly to the cyclable lithium loss induced by the anode SEI growth. In the stabilization stage, the anode SEI growth slows down as it gets thicker, the cathode Mn dissolution-induced capacity loss outpaces cyclable lithium loss, and the cathode becomes more intercalated at the end of discharge. In the saturation stage, cathode capacity degrades further and becomes the limiting factor, the cyclable lithium is shifted to the anode and the cathode reaches end-of-discharge saturation due to the severe cathode capacity fade. This study shows that the cyclable lithium loss and the cathode capacity loss are the two major contributors to the cell capacity fade, and the interaction between them determines the cell capacity.
 [DOI: 10.1149/2.040310jes]

Manuscript submitted May 6, 2013; revised manuscript received July 29, 2013. Published August 20, 2013.

Energy security and climate change challenges provide a strong impetus for the development of electric vehicles (EV) and hybrid electric vehicles (HEV).[1,2] Lithium ion batteries are one of the most important components of the EVs and HEVs. One of the most important topics is the degradation, or aging process, of the cells during operation. A substantial amount of work has gone into understanding capacity fade through experiments and theoretical/numerical studies. Ramadass et al.[3] carried out a complete capacity fade analysis for the Sony 18650 cells after hundreds of cycles. They divided the capacity fade into rate capability loss as well as primary and secondary active material losses. However, they proposed no model to quantitatively explain the capacity fade due to different mechanisms. Safari et al.[4] proposed a multimodal physics-based aging model to predict the capacity fade for Li-ion batteries. They assumed that capacity fade stems mainly from solid electrolyte interphase (SEI) growth on the anode, and that lithium ion consumption during SEI growth was the main contributor to cycling degradation. Zhang et al.[5] developed a single-particle model which they calibrated against the cycling data to study the parameter trajectories. They suggested that there were probably different stages of capacity fade in the lithium ion battery. However, they proposed no degradation model to quantitatively study the degradation process.

The studies above have attempted to elucidate capacity fade by focusing on specific mechanisms, not by regarding all the key mechanisms together. Because each mechanism is coupled to each other, it is important to consider all of them and their interactions simultaneously. In this way, the whole life of a battery cell can be predicted, and its pattern can be analyzed. From this point of view, an attempt is made in this study to develop a physics-based model to predict the capacity fading process. There is a number of degradation mechanisms associated with cell degradation.[6] The most known processes leading to capacity fade in the Li-ion batteries are SEI growth and manganese deposition on the anode electrode, as well as manganese dissolution, electrolyte oxidation and salt decomposition on the cathode electrode. Quantifying all these degradation processes will improve prediction of cell capacity during operations.

It is now well known that the carbonaceous lithium-insertion electrodes experience a significant amount of irreversible capacity loss during the initial charging cycles.[7] Irreversible capacity loss during the first few cycles is thought to result from the formation of the SEI layer on the surface of the carbon. On the anode surface, the SEI layer continues growing and dissolving due to the continuous reduction of the electrolyte and the reformation of the SEI layers. The process consumes the cyclable lithium ions, which leads to irreversible capacity loss in the lithium ion batteries. SEI formation can remove a significant amount of the cyclable lithium depending on the type of carbon used. For the graphitic materials such as Osaka Gas mesocarbon micobeads (MCMB) irreversible capacity is as low as 8 to 15%, whereas for the hard carbons it can be as high as 50% of the reversible capacity.[6]

Lithium Manganese Oxide (LMO) spinel has been extensively investigated during the past 10 years. LMO spinel is a good cathode material due to its economic and non-toxic features. However, capacity degradation during cycling becomes an obstacle for its higher market share. Several degradation mechanisms, such as surface film formation, electrolyte decomposition, and Mn dissolution have been proposed for the capacity loss. Jang et al.[8] stated that manganese dissolution is the primary reason for capacity fade in the LMO spinal cathode. They also reported that the solvent molecules are electrochemically oxidized and that spinel dissolution is promoted by the acids generated as a result of solvent oxidation.[9] Their results revealed the important link between the generation of protons and manganese dissolution. In order to quantitatively study LMO degradation, Park et al.[10] developed a mathematical model of LMO cathode degradation based on the Mn(III) disproportionation mechanism.[11] Later, Dai et al.[12] proposed a capacity fade model including acid generation from two side reactions (solvent oxidation and the $LiPF_6$ decomposition); acid-promoted Mn dissolution was also studied. Although the dissolution of Mn in the LMO spinel cathode is an important factor for capacity fade, chemical analytical results indicate that capacity loss caused solely by Mn^{2+} dissolution accounts for only 34% and 23% of the overall capacity loss at 50°C and room teperature, respectively.[13] Not only does Mn dissolution lead to cathode degradation, but the reduction reaction of Mn^{2+} on the negative electrode causes additional capacity fade as well.[14]

In this paper, we present a side-reaction coupled electrochemical model for the capacity fade analysis of lithium ion batteries. This side-reaction coupled electrochemical model includes the major side reactions: anode SEI growth, Mn deposition, cathode Mn dissolution, electrolyte oxidation and salt decomposition. The cell internal resistance increase due to SEI formation on the surface of anode is also included. The effects of different degradation mechanisms on capacity fade and battery performance are studied quantitatively. As a result, it is found that the degradation process of a Li-ion cell can be divided into three main stages: acceleration, stabilization and saturation. This analysis clearly explains the role and process of each degradation mechanism on the life of the battery at each stage.

Model Development

The battery system considered in this study is a graphite/LMO full cell, which consists of a 150 μm anode, a 30 μm separator and

[z]E-mail: weilu@umich.edu

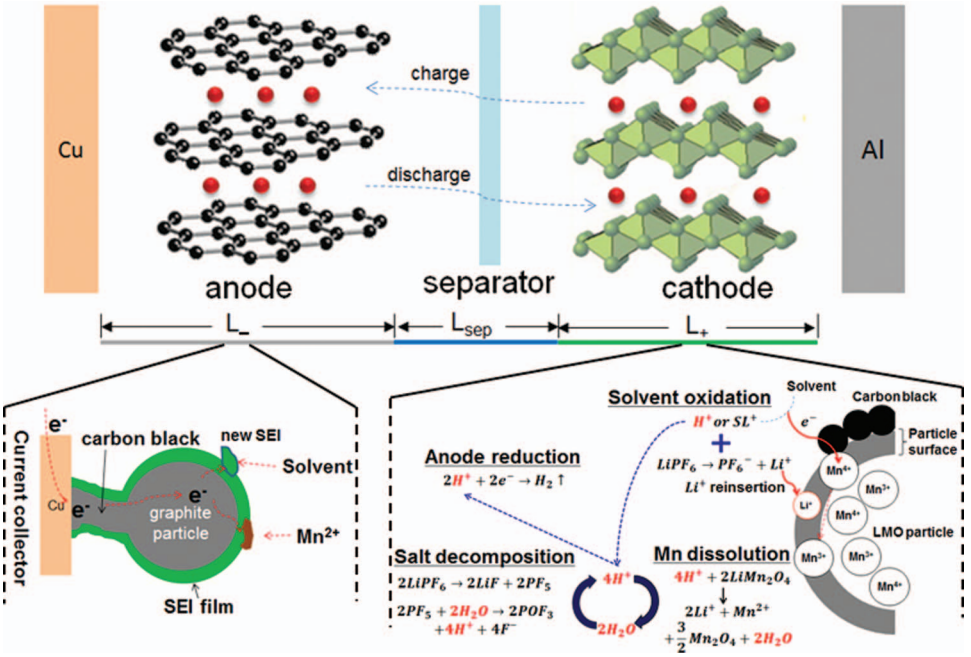

Figure 1. A schematic diagram of side reactions coupled with the cell level framework. The left bottom figure illustrates side reactions on the anode, including SEI formation and Mn deposition. The right bottom figure illustrates side reactions on the cathode, including salt decomposition, solvent oxidation, and Mn dissolution.

a 110 μm cathode in 1 M $LiPF_6$ ethylene carbonate (EC) / dimethyl carbonate (DMC) electrolyte. In order to explore the long-term degradation pattern, each side reaction is coupled to the electrochemical cell-level model. This model consists of two levels: the particle level and cell level. The particle-level modeling describes side reactions on both anode and cathode electrodes. The cell-level electrochemical model based on porous-electrode theory describes the lithium ion transportation process during charge and discharge.[15] The two levels are coupled through the local reaction current based on charge conservation.

The following sections introduce details of the modeling work and are divided into three parts. The first part introduces side reactions on the anode surface, which are mainly responsible for the cyclable lithium ion loss. The second part focuses on the side reactions on the cathode, which lead to the active material loss and capacity fade of the cathode. Finally, the side reactions are coupled to a cell-level electrochemical model for studying cell degradation.

Part I: modeling of side reaction at anode.— Several side reactions occur on the surface of the anode particles. Examples of these include SEI formation, metallic manganese deposition[16] and the reduction of a small amount of H^+ generated from solvent oxidation and salt decomposition.[12] A particle-level model is developed to describe the side reactions when the SEI layer is growing. The impact of the SEI layer on the side reactions is included in the model. As shown in the left bottom of Fig. 1, the anode particle is covered by a thin SEI layer which can vary from a few nm to hundreds nm depending on the cycling conditions and the compositions of the system.

In a fresh cell the SEI layer is not yet formed, so the side reaction rate is controlled only by Butler-Volmer equations which consider the reactant concentration and electric potential. As the SEI grows thicker, the side reactions are slowed down because the electrolyte diffusion through the SEI film to the graphite surface is limited.[4] The SEI film growth curves from numerical simulations based on detailed chemistry model[17] and solvent-diffusion model,[4] and also the experimental measurements based on spectroscopic ellipsometry[18] clearly show a decaying SEI growth rate as SEI film thickness increases. The decaying growth rate with respect to the thickness of the SEI film can be well approximated by an exponential decay function of

$$R(\delta) \approx e^{-\lambda\delta}, \qquad [1]$$

where $R(\delta)$ is the limiting factor which ranges from 0 to 1, δ is the thickness of the SEI layer and λ is the limiting coefficient.

The side reation rates limited by the SEI layer can be expressed by

$$i_{side} = R(\delta)\cdot i^*_{side} = e^{-\lambda_{side}\delta}\cdot i_0^{side}\left\{\exp\left[\frac{\alpha_a^{side} nF}{RT}\left(\phi-\phi_{eq}\right)\right] - \exp\left[-\frac{\alpha_c^{side} nF}{RT}(\phi-\phi_{eq})\right]\right\}, \qquad [2]$$

where i_{side} is the side reaction limited by the SEI layer, i^*_{side} is the original side reaction rate without SEI limitation, λ_{side} is the limiting coefficient of the side reaction, i_0^{side} is the exchange current density, α_a^{side} is the anodic charge transfer coefficent, α_c^{side} is the cathodic charge transfer coeffcient, n is the number of electrons involved in the reaction, F is the Faraday constant, R is the gas constant, T is the absolute temperature, ϕ is the electric potential and ϕ_{eq} is the equlibirum potential for the side reaction.

SEI formation.— There is continuous SEI formation reaction between the lithiated graphite and the electrolyte solvent. This continuous SEI growth leads to a gradual consumption of the cyclable lithium and an increase in electrode impedance upon cycling.

The electrolyte reduction reactions occurring on the graphite surface are very similar to those on the lithium metal.[19] Aurbach et al.[19] stated that the lithium ethylene dicarbonate $(CH_2OCO_2Li)_2$ and ethylene gas resulting from a one-electron reduction process of EC are the dominant products in the SEI formation. In this study, lithium ethylene dicarbonate $(CH_2OCO_2Li)_2$ is considered to be the main component of the SEI layer.

The following equations show the SEI formation process. The rate-determining step is considered to be the radical anion formation process[4] shown in Eq. 3.

$$EC + e^-(graphite) \rightarrow EC^- \qquad [3]$$

$$EC^- + EC^- \rightarrow (O_2CO)^-(CH_2)_2(O_2CO)^- + C_2H_4 \uparrow \quad [4]$$

$$EC^- + EC + e^-(graphite) \rightarrow (O_2CO)^-(CH_2)_2(O_2CO)^- + C_2H_4 \uparrow \quad [5]$$

$$(O_2CO)^-(CH_2)_2(O_2CO)^- + 2Li^+ \rightarrow Li^+(O_2CO)^-(CH_2)_2(O_2CO)^-Li^+ \quad [6]$$

The reaction rate of the radical anion formation process at the interface of the graphite and the electrolyte, i^*_{SEI}, is expressed by[4]

$$i^*_{SEI} = -Fk_{SEI}c_{EC}\exp[-\frac{\alpha_c^{SEI}F}{RT}(\phi_1 - \phi_2)], \quad [7]$$

where k_{SEI} is the reaction rate constant of SEI, c_{EC} is the solvent concentration, α_c^{SEI} is the cathodic charge transfer coeffcient, ϕ_1 is the solid-phase potential, and ϕ_2 is the solution-phase potential.

As mentioned above, as the SEI grows thicker, the reaction rate slows down. The modified SEI side reaction rate, i_{SEI}, is given by

$$i_{SEI} = R(\delta)\cdot i^*_{SEI} = -e^{-\lambda_{SEI}\delta}Fk_{SEI}c_{EC}\exp\left[-\frac{\alpha_c^{SEI}F}{RT}(\phi_1 - \phi_2)\right]. \quad [8]$$

The growth rate of the SEI layer due to the accumulation of lithium ethylene dicarbonate is related to the side-reaction current density by[4]

$$\frac{d\delta}{dt} = -\frac{i_{SEI}}{2F}\frac{M_{SEI}}{\rho_{SEI}} \quad [9]$$

where t is time, M_{SEI} is the molecular weight of SEI, and ρ_{SEI} is the SEI density.

Manganese deposition and acid reduction.— The deposition of Mn particles on the lithium metal after cycling was confirmed through EDX analysis.[20,21] Komaba et al.[14] conducted cycling experiments in 1 M $LiClO_4$ EC/DEC solution where Mn was added before and during the cycling. The discharge capacity will severely decrease due to Mn^{2+} reduction on the anode surface. The Mn deposition is believed to decrease the cyclable lithium ions because manganese deposition consumes electrons that are supposed to be coupled to lithium ions during the intercalation process. This side reaction is expressed by

$$Mn^{2+} + 2e^- \rightarrow Mn(s), \quad [10]$$

which implies that Mn deposition on the graphite anode will reduce the amount of cyclable lithium ions in the cell.

Because the reaction is controlled by electrical charge transfer, the Mn deposition process follows the Butler Volmer expression,[12] which can be expressed in the form of

$$i^*_{Mn\_dep} = -Fk_{Mn\_dep}c_{Mn^{2+}}\exp\left[-\frac{\alpha_c^{Mn\_dep}2F}{RT}(\phi_1 - \phi_2)\right], \quad [11]$$

where $i^*_{Mn\_dep}$ is the Mn deposition rate, k_{Mn_dep} is the reaction rate constant, $c_{Mn^{2+}}$ is the Mn^{2+} concentration, and $\alpha_c^{Mn\_dep}$ is a cathodic charge transfer coeffcient in the process.

The Mn deposition is also considered to be affected by the SEI thickness. As the SEI grows thicker, the Mn deposition rate should decrease, giving

$$i_{Mn\_dep} = R(\delta)\cdot i^*_{Mn\_dep} = -e^{-\lambda_{Mn\_dep}\delta}Fk_{Mn\_dep}c_{Mn^{2+}} \times \exp\left[-\frac{\alpha_c^{Mn\_dep}2F}{RT}(\phi_1 - \phi_2)\right]. \quad [12]$$

The protons generated from electrolyte oxidation and salt decomposition could also be consumed at the anode surface via[6]

$$H^+ + e^- \rightarrow \frac{1}{2}H_2(g). \quad [13]$$

The reaction is controlled by electrical charge transfer and the reaction rate can be expressed by

$$i_{H_2} = R(\delta)\cdot i^*_{H_2} = -e^{-\lambda_{H_2}\delta}F\,k_{H_2}c_{H^+}\exp\left[-\frac{\alpha_c^{H_2}F}{RT}(\phi_1 - \phi_2)\right], \quad [14]$$

where k_{H_2} is the reaction rate constant, c_{H^+} is the H^+ concentration, and $\alpha_c^{H_2}$ is a cathodic charge transfer coeffcient.

When the cell is being discharged, the potential difference $\phi_1 - \phi_2$ is large, giving a very small reaction rate. Therefore, we assume that there is no reduction/oxidation reactions for H^+ and Mn^{2+} during discharge.[12]

Part II: modeling of side reaction at cathode.— Important side reactions in the cathode electrode include electrolyte oxidation, salt decomposition and Mn dissolution.[22,23] Further, these side reactions are coupled with each other. The protons generated as a result of solvent oxidation and salt decomposition play a key role in Mn dissolution.[9] The generated protons attack the active material on the cathode surface. This Mn dissolution process can be expressed by[9,12,24]

$$4H^+ + 2LiMn_2O_4 \rightarrow 2Li^+ + Mn^{2+} + \frac{3}{2}Mn_2O_4 + 2H_2O. \quad [15]$$

The reaction rate is controlled by the proton concentration in the cathode because of the high content of LMO in the cathode and the small concentration of protons. Part of Mn^{2+} forms composites such as MnF_2 in the SEI layer on the cathode surface,[22] the dissolved Mn^{2+} is hypothesized to be a fraction of the reaction product, and is expressed by

$$i_{Mn\_dis} = f_{Mn\_dis}i_{Mn\_react} = f_{Mn\_dis}Fk_{dis}c_{H^+}, \quad [16]$$

where i_{Mn_dis} is the Mn dissolution rate, f_{Mn_dis} is the fraction coefficient, i_{Mn_react} is the reaction rate, and k_{dis} is the reaction rate constant for the acid attack on the active material.

The protons originate from two main sources. The first source is solvent oxidation,[9,12,24]

$$Solvent \xrightarrow{oxidation} SL_o + H^+(or\,SL^+) + e^-, \quad [17]$$

where SL_o and SL^+ represent the solvent oxidation products. The reaction is controlled by electrical charge transfer, and the solvent oxidation rate per volume, j_{oxid}, can be expressed by the Butler-Volmer equation,[12]

$$j_{oxid} = a_c i_0^{sol}\left\{\exp\left[\frac{\alpha_a^{sol}F}{RT}\eta_{oxid}\right] - \exp\left[-\frac{\alpha_c^{sol}F}{RT}\eta_{oxid}\right]\right\}, \quad [18]$$

$$\eta_{oxid} = \phi_1 - \phi_2 - U^{eq}_{oxid}, \quad [19]$$

where a_c is the surface area per unit volume for the solvent oxidation, i_0^{sol} is the exchange current density, α_a^{sol} is the anodic charge transfer coefficient, α_c^{sol} is the cathodic charge transfer coefficient, and U^{eq}_{oxid} is the equilibrium potential of the side reaction.

An anodic Tafel expression can be used to describe the rate if the decomposition reaction is considered irreversible, where

$$j_{oxid} = a_c i_0^{sol}\exp\left(\frac{\alpha_a^{sol}F}{RT}\eta_{oxid}\right). \quad [20]$$

The proton generation rate per volume by solvent oxidation is assumed to be a fraction of the oxidation current,

$$j^{oxid}_{H^+} = f_{H^+}\cdot j_{oxid}, \quad [21]$$

where $f_{H^+}$is a fraction coefficient.

The surface area for the solvent reaction should be adjusted according to the carbon content since solvent oxidation occurs mostly on the surface of the conductive carbon black.[25] We assume that a_c is related to the carbon content X_c% (weight percentage) by

$$a_c = \frac{X_c}{X_c^{ref}}a_c^{ref}, \quad [22]$$

where X_c^{ref} represents the carbon content for a preset value, and a_c^{ref} is the value of a_c corresponding to the preset carbon content, X_c^{ref}.

The other source for the proton is the decomposition of $LiPF_6$,[23]

$$LiPF_6 \rightarrow LiF + PF_5, \quad [23]$$

where the product PF_5 reacts with water to form HF, namely

$$PF_5 + H_2O \rightarrow POF_3 + 2HF. \quad [24]$$

The proton production rate per volume due to $LiPF_6$ decomposition is given by[23]

$$j_{H^+}^{salt} = Fk_{decom}(c_{H_2O})^2 c_{LiPF_6}, \quad [25]$$

where k_{decom} is the reaction coefficient, c_{H_2O} is the water concentration in the electrolyte, and c_{LiPF_6} is the $LiPF_6$ concentration in the electrolyte. Due to the high ionization of $LiPF_6$, the concentration c_{LiPF_6} can be approximated by c_{Li^+}.

The effect of the potential on the transport of Mn^{2+} and H^+ is neglected due to the extremely low concentrations of these species. Therefore, the migration term is neglected, and only the diffusion law applies in the mass conservation of H^+ and Mn^{2+}.[12]

The overall reaction and diffusion process is summarized in the right bottom of Fig. 1. The mass conservation for H^+ is expressed by

$$\varepsilon_2^{pos}\frac{\partial c_{H^+}}{\partial t} = \nabla\cdot\left(D_{H^+}^{eff}\nabla c_{H^+}\right) + \frac{1}{F}\left(j_{H^+}^{oxid} + j_{H^+}^{salt} - 4a_s^{pos}i_{Mn\_react}\right), \quad \text{positive electrode} \quad [26]$$

$$\varepsilon_2^{sep}\frac{\partial c_{H^+}}{\partial t} = \nabla\cdot\left(D_{H^+}^{eff}\nabla c_{H^+}\right) + \frac{j_{H^+}^{salt}}{F}, \quad \text{separator} \quad [27]$$

$$\varepsilon_2^{neg}\frac{\partial c_{H^+}}{\partial t} = \nabla\cdot\left(D_{H^+}^{eff}\nabla c_{H^+}\right) + \frac{1}{F}\left(j_{H^+}^{salt} + a_s^{neg}i_{H_2}\right), \quad \text{negative electrode} \quad [28]$$

$$\text{Boundary conditions}: \left.\frac{\partial c_{H^+}}{\partial x}\right|_{x=0} = \left.\frac{\partial c_{H^+}}{\partial x}\right|_{x=L} = 0, \quad [29]$$

where ε_2 is the electrolyte phase volume fraction, $D_{H^+}^{eff}$ is the effective diffusivity of H^+, a_s^{pos} and a_s^{neg} are the active surface area per unit electrode volume on the postive (pos) electrode and negative (neg) electrode, respectively, and L represents the cell thickness including the anode, seperator and cathode.

The mass conservation for Mn^{2+} in the electrolyte is expressed by:

$$\varepsilon_2^{pos}\frac{\partial c_{Mn^{2+}}}{\partial t} = \nabla\cdot\left(D_{Mn^{2+}}^{eff}\nabla c_{Mn^{2+}}\right) + \frac{1}{F}a_s^{pos}i_{Mn\_dis}, \quad \text{positive electrode} \quad [30]$$

$$\varepsilon_2^{sep}\frac{\partial c_{Mn^{2+}}}{\partial t} = \nabla\cdot\left(D_{Mn^{2+}}^{eff}\nabla c_{Mn^{2+}}\right), \quad \text{separator} \quad [31]$$

$$\varepsilon_2^{neg}\frac{\partial c_{Mn^{2+}}}{\partial t} = \nabla\cdot\left(D_{Mn^{2+}}^{eff}\nabla c_{Mn^{2+}}\right) + \frac{1}{F}a_s^{neg}i_{Mn\_dep}, \quad \text{negative electrode} \quad [32]$$

$$\text{Boundary condition}: \left.\frac{\partial c_{Mn^{2+}}}{\partial x}\right|_{x=0} = \left.\frac{\partial c_{Mn^{2+}}}{\partial x}\right|_{x=L} = 0, \quad [33]$$

where $c_{Mn^{2+}}$ is the concentration of Mn^{2+} and $D_{Mn^{2+}}^{eff}$ is the effective diffusivity.

The mass conservation for H_2O in the electrolyte is expressed by

$$\varepsilon_2^{pos}\frac{\partial c_{H_2O}}{\partial t} = \nabla\cdot\left(D_{H_2O}^{eff}\nabla c_{H_2O}\right) + \frac{1}{F}\left(2a_s^{pos}i_{Mn\_react} - j_{H^+}^{salt}\right), \quad \text{positive electrode} \quad [34]$$

$$\varepsilon_2^{sep}\frac{\partial c_{H_2O}}{\partial t} = \nabla\cdot\left(D_{H_2O}^{eff}\nabla c_{H_2O}\right) - \frac{j_{H^+}^{salt}}{F}, \quad \text{separator} \quad [35]$$

$$\varepsilon_2^{neg}\frac{\partial c_{H_2O}}{\partial t} = \nabla\cdot\left(D_{H_2O}^{eff}\nabla c_{H_2O}\right) - \frac{j_{H^+}^{salt}}{F}, \quad \text{negative electrode} \quad [36]$$

$$\text{Boundary condition}: \left.\frac{\partial c_{H_2O}}{\partial x}\right|_{x=0} = \left.\frac{\partial c_{H_2O}}{\partial x}\right|_{x=L} = 0, \quad [37]$$

where $D_{H_2O}^{eff}$ is the effective diffusivity of H_2O.

The Mn dissolution-induced active material loss alone cannot explain the overall capacity loss. Xia et al.[13] reported that the measured capacity losses caused by Mn dissolution are only 34% and 23% of the overall capacity loss at 50°C and room teperature, respectively. It is suspected that the other loss of the overall capacity is due to the Mn dissolution-induced contact-resistance increase, particle structure distortion and LMO particle isolation from the conductive nework.[26]

In our study, contact-resistance increase and active material loss are modeled based on the volume fraction change of the LMO cathode. Accounting for the acid-induced Mn dissolution, the volume fraction of the solid phase, ε_1, at the cathode is given by[12]

$$\frac{\partial \varepsilon_1^{pos}}{\partial t} = -\frac{a_s^{pos}i_{Mn\_react}\overline{V}}{F}, \quad [38]$$

where $\overline{V}$ is the molar volume of LMO.

The effective conductivity of the solid phase, k_1^{eff}, relates to the volume fraction by

$$k_1^{eff} = k_1(\varepsilon_1)^p, \quad [39]$$

wherei k_1 is the solid phase conductivity, and p is the Bruggeman porosity exponent.

As disccused above, cathode capacity fade stems from Mn dissolution-induced active material loss, contact-resistance increase, particle structure distortion and particle isolation. The active material loss and contact-resistance increase can be reflected in the cell level model by Eq. 38 and Eq. 39. However, in order to reflect the capacity fade due to particle structure distortion and particle isolation in the cell level model, a term called usable volume fraction, $\varepsilon_{usable}^{pos}$, is introduced here. The solid phase volume fraction, ε_1^{pos}, accounts for all the active and inactive (isolated and distorted) particles in the solid phase, while the usable volume fraction, $\varepsilon_{usable}^{pos}$, accounts for only the connected active particles in the solid phase and therefore can reflect the capacity fade due to particle isolation and structure distortion. Normally, $\varepsilon_{usable}^{pos}$, is smaller than ε_1^{pos} except at the initial state where they have the same value. The change of the usable volume fraction is hypothesized to be propotional to the change of the solid phase volume fraction, namely

$$\varepsilon_{usable0}^{pos} = \varepsilon_{1,ini}^{pos} \text{ at } t = 0, \quad [40]$$

$$\frac{d\varepsilon_{usable}^{pos}}{dt} = k_{iso}\frac{d\varepsilon_1^{pos}}{dt}, \quad [41]$$

where k_{iso} is a coefficient.

As a LMO particle becomes isolated from the conductive network or distorted due to Mn dissolution, the effective capacity per unit electrode volume decreases. The maximum concentration of Li per unit electrode volume also decreases,

$$c_{el,\max}^{pos} = \varepsilon_{usable}^{pos}c_{1,max}^{pos}, \quad [42]$$

$$c_{el}^{pos} = \varepsilon_1^{pos}c_1^{pos}, \quad [43]$$

where $c_{el,\max}^{pos}$ is the maximum amount of lithium per unit electrode volume, $c_{1,max}^{pos}$ is the maximum lithium concenctration in the solid phase, c_{el}^{pos} is the amount of lithium per unit electrode volume, and c_1^{pos} is the lithium concenctration in the solid phase. Therefore, the state of charge (SOC) of the electrode can be calculated by

$$SOC^{pos} = c_{el}^{pos}/c_{el,\max}^{pos}. \quad [44]$$

Table I. An overview of key equations employed in the degradation model.

Cell level modeling	Boundary conditions
Charge	
Electrolyte phase $\frac{\partial}{\partial x}\left(k_2^{eff}\frac{\partial \phi_2}{\partial x}\right)-\frac{\partial}{\partial x}\left(k_{2D}^{eff}\frac{\partial}{\partial x}\ln c_2\right)+j_{loc}=0$	$\left.\frac{\partial \phi_2}{\partial x}\right\|_{x=0}=\left.\frac{\partial \phi_2}{\partial x}\right\|_{x=L}=0$
Solid phase $\frac{\partial}{\partial x}\left(k_1^{eff}\frac{\partial \phi_1}{\partial x}\right)-j_{loc}=0$	$-k_1^{eff}\left.\frac{\partial \phi_1}{\partial x}\right\|_{x=0}=k_1^{eff}\left.\frac{\partial \phi_1}{\partial x}\right\|_{x=L}=\frac{I}{A},\ \left.\frac{\partial \phi_1}{\partial x}\right\|_{x=L_-}=\left.\frac{\partial \phi_1}{\partial x}\right\|_{x=L_-+L_{sep}}=0$
Species	
Electrolyte phase	
$\frac{\partial(\varepsilon_2 c_2)}{\partial t}=\frac{\partial}{\partial x}\left(D_2^{eff}\frac{\partial c_2}{\partial x}\right)+\frac{1-t_+^0}{F}j_{loc}$ (Anode and Separator)	$\left.\frac{\partial c_2}{\partial x}\right\|_{x=0}=\left.\frac{\partial c_2}{\partial x}\right\|_{x=L}=0$
$\frac{\partial(\varepsilon_2 c_2)}{\partial t}=\frac{\partial}{\partial x}\left(D_2^{eff}\frac{\partial c_2}{\partial x}\right)+\frac{1-t_+^0}{F}j_{loc}+\frac{(2a_s^{pos}i_{Mn\_react}-j_{oxid})}{F}$ (Cathode)	
Solid phase $\frac{\partial(c_1)}{\partial t}=\frac{D_1}{r^2}\frac{\partial}{\partial r}\left(r^2\frac{\partial c_1}{\partial r}\right)$	$\left.\frac{\partial c_1}{\partial r}\right\|_{r=0}=0,\ D_1\left.\frac{\partial c_1}{\partial r}\right\|_{r=R_s}=-\frac{j_{Li}}{a_s F}$
Side reaction modeling	**Equations**
Anode SEI growth	$i_{SEI}=R(\delta)\cdot i_{SEI}^*=-e^{-\lambda_{SEI}\delta}Fk_{SEI}c_{EC}\exp[-\frac{\alpha_c^{SEI}F}{RT}(\phi_1-\phi_2)]$
Anode Manganese deposition	$i_{Mn\_dep}=R(\delta)\cdot i_{Mn\_dep}^*=-e^{-\lambda_{Mn\_dep}\delta}Fk_{Mn\_dep}c_{Mn^{2+}}\exp\left[-\frac{\alpha_c^{Mn\_dep}2F}{RT}(\phi_1-\phi_2)\right]$
Anode hydrogen gas	$i_{H_2}=R(\delta)\cdot i_{H_2}^*=-e^{-\lambda_{H_2}\delta}Fk_{H_2}c_{H^+}\exp\left[-\frac{\alpha_c^{H_2}F}{RT}(\phi_1-\phi_2)\right]$
Cathode Mn dissolution	$i_{Mn\_react}=Fk_{dis}c_{H^+}$
Cathode electrolyte oxidation	$j_{oxid}=a_c i_0^{sol}\exp\left(\frac{\alpha_a^{sol}F}{RT}\eta_{oxid}\right)$
Cathode salt decomposition	$j_{H^+}^{salt}=Fk_{decom}(c_{H_2O})^2 c_{LiPF_6}$

The lithium concentration in the electrode decreases as Mn dissolution induced particle distortion and isolation increases.

Part III: Side reaction coupled cell level electrochemical model.— As shown in Fig. 1, a typical lithium ion cell consists of two porous composite electrodes, an ionic conductive separator and copper and aluminum current collectors. Newman's porous composite electrode model[27] is used here as the basic cell level framework. The cell level model consists of three domains: the negative composite electrode, the separator, and the positive composite electrode. The composite electrodes consist of active material (Li_xC_6 for the anode, $Li_yMn_2O_4$ for the cathode), electrolyte solution ($LiPF_6$ 1M EC/DMC) and a small amount of conductive additive (carbon black) and binder (PVDF). The mass and charge are conserved in the cell. The total lithium intercalation and deintercalation current per volume j_{loc}, is taken into account by the Butler-Volmer equation,

$$j_{loc}=a_s i_0\left\{\exp\left[\frac{\alpha_a F}{RT}\left(\eta-\frac{R_{SEI}}{a_s}j_{loc}\right)\right]-\exp\left[-\frac{\alpha_c F}{RT}\left(\eta-\frac{R_{SEI}}{a_s}j_{loc}\right)\right]\right\} \quad [45]$$

$$\eta=\phi_1-\phi_2-U \quad [46]$$

$$R_{SEI}=k_{res}\delta \quad [47]$$

where j_{loc} is the local reaction current, a_s is the active surface area per unit electrode volume, i_0 is the exchange current density, α_a is the anodic charge transfer coefficent, α_c is the cathodic charge transfer coeffcient, R_{SEI} is the resistance of the SEI layer, U is the open-circuit potential, and k_{res} is the SEI resistivity.

In order to couple the side-reaction particle-level model to Newman's cell level model, the side-reaction induced cyclable lithium loss should be added or subtracted from the lithium intercalation or deintercalation. On the anode, the side reactions are coupled to the cell level model through the following equations:

$$j_{Li}=j_{loc}-j_{side} \quad [48]$$

$$j_{side}=a_s^{neg}(i_{SEI}+i_{H_2}+i_{Mn\_dep}) \quad [49]$$

where j_{Li} is the current density of lithium intercalation or deintercalation, i_{SEI} is the lithium loss due to SEI growth, i_{H_2} is the lithum loss from the hydrogen gas, and i_{Mn_dep} represents the lithium loss by Mn deposition.

On the cathode, the side reactions are coupled to the cell level model by

$$j_{Li}=j_{loc}+2a_s^{pos}i_{Mn\_react}-j_{oxid} \quad [50]$$

where i_{Mn_react} is lithum loss due to acid attack and j_{oxid} is lithium reinsertion due to electrolyte oxidation.

The equations used in the degradation model are summarized in Table I. The side reaction equations are divided into the anode side and cathode side. The battery model parameters are summarized in Table II. The meanings of the parameters in Newman models can be found in the reference.[27] Table III lists the key parameters for the side reactions. More details on the parameters can be found in the reference.[4,12]

Results and Discussion

The dynamic process of cell degradation and the effects of each different degradation mechanism on battery capacity fade during cycling are investigated using the developed model. A cycling condition is simulated based on constant current/constant voltage (CCCV): the cell is charged with 1C rate until the cutoff voltage of 4.1 V. Next, the voltage is held until the current drops down to 0.1C. Next, the cell is discharged to 3.4 V at 1C, held at 3.4 V until the current drops down to 0.1C. The following sections show the details of capacity fade during cycling and the analysis of capacity fade based on the degradation mechanisms described previously.

Capacity fade during cycling.— In order to trace cyclable lithium loss through the whole cell life from factory assemblage to cell failure, the simulation starts from the fresh cell condition, in which the cell is composed of an empty graphite anode and a fully liathiated LMO cathode. The initial SOCs of the negative electrode and the positive electrode are set to 0.01 and 0.99, respectively, in order to represent the fresh state of the cell.

Table II. Battery parameters.

Parameter	Negative electrode	Separator	Positive electrode
Electrode thickness (m)	150×10^{-6}	30×10^{-6}	110×10^{-6}
Particle radius R_s (m)	12.5×10^{-6}		8.5×10^{-6}
Active material volume fraction ε_1	0.471		0.297
Polymer and conductive filler volume fraction ε_3	0.172		0.259
Porosity (electrolyte phase volume fraction) ε_2	0.357	1	0.444
Solid phase conductivity k_1 (S/m)	100		3.8
Effective conductivity of solid phase k_1^{eff} (S/m)	$k_1^{eff} = k_1(\varepsilon_1)^p$		$k_1^{eff} = k_1(\varepsilon_1)^p$
Maximum solid phase concentration $c_{1,max}$ (mol/m^3)	26390		22860
Solid phase Li diffusion coefficient D_1 (m^2/s)	3.9×10^{-14}		1×10^{-13}
Initial electrolyte concentration (mol/m^3)	1000	1000	1000
Li transference number t_+^0	0.363	0.363	0.363
Electrolyte phase ionic conductivity k_2 (S/m)[c]		$k_2(c_2)$ curve	
Effective electrolyte phase ionic conductivity k_2^{eff} (S/m)		$k_2^{eff} = k_2(\varepsilon_2)^p$	
Electrolyte phase Li diffusion coefficient D_2 (m^2/s)	7.5×10^{-11}	7.5×10^{-11}	7.5×10^{-11}
Effective electrolyte phase Li diffusion coefficient D_2^{eff} (m^2/s)		$D_2^{eff} = D_2(\varepsilon_2)^p$	
Effective electrolyte phase Li diffusion conductivity k_{2D}^{eff} (A/m)		$k_{2D}^{eff} = \frac{2RTk_2^{eff}}{F}(1 - t_+^0)(1 + \frac{d \ln f_-^+}{d \ln c_2})$	
Electrolyte activity coefficient f_-^+	1	1	1
Bruggeman porosity exponent p	1.5	1.5	1.5
Charge transfers coefficient α_a, α_c	0.5		0.5
Reaction rate coefficient k_0 (m/s)	2×10^{-11}		2×10^{-11}
Exchange current density i_0 (A/m^2)		$Fk_0c_2^{\alpha_a}(c_{1,max} - c_{1,s})^{\alpha_a}c_{1,s}^{\alpha_c}$	
Active surface area per unit electrode volume a_s (1/m)	$\frac{3\varepsilon_1}{R_s}$		$\frac{3\varepsilon_1}{R_s}$
Faraday constant F (C/mol)		96485.3415	
Initial electrode SOC (fresh cell)	0.01		0.99
Negative electrode equilibrium potential U_(V)[c]	U_$(c_{1,s}/c_{1,max})$ curve		
Positive electrode equilibrium potential U$_+$(V)[c]			U$_+(c_{el}^{pos}/c_{el,max}^{pos})$ curve

[c]Curves in Appendix

Figure 2 shows the discharge capacity fade during cycling from our model prediction. The capacity degradation of the cell can be divided into three stages: acceleration, stabilization and saturation. Spotnitz studied the cycle life data from many manufacturers.[28] These data showed that the rate of capacity fade was initially high, but slowed down quickly. After several hundreds of cycles the rate of capacity fade started a rapid increase. This degradation pattern is consistent with the degradation stages reported by our model. In the acceleration stage, capacity fade is quite fast due to SEI formation on the anode surface. SEI formation can remove a significant amount of cyclable lithium. For the graphitic materials such as MCMB, the irreversible capacity ranges between 8% and 15%.[6] In our simulation, the capacity fade in the acceleration stage is about 10%, which is close to the experimental values.[6] As the SEI grows thicker, the reaction rate slows down due to the isolation effect of SEI layer. The cyclable lithium loss also slows down, and the battery enters the stabilization stage. In this stage, battery performance is relatively stable, and capacity decreases slowly. Instead of cyclable lithium loss, the capacity loss of the cathode due to Mn dissolution becomes a main contributor to capacity fade. As Mn dissolution develops further, the cathode capacity is insufficient to contain all the cyclable lithium in the system and the cathode is almost fully intercalated at the end of discharge. At this point, the cell enters the saturation stage. Due to the steepness of the cathode voltage curve at high depth of discharge (DOD), the battery discharge process reaches the cutoff voltage earlier.

The capacity fade is also reflected in the discharge curves of aged graphite/LMO cell during 900 cycles as shown in Fig. 3. In the initial cycles where SEI formation-induced cyclable lithium loss is the dominant contributor to the cell capacity fade, a quick shift of the

Table III. Parameters of side reactions.

Parameter	Value	Parameter	Value
k_{SEI}	6×10^{-10} m/s	α_a^{sol}	0.5
c_{EC}	4541 mol/m^3	U_{oxid}^{eq}[a]	4.1 V
λ_{SEI}[a]	1.2×10^7 1/m	f_{H^+}[a]	15%
α_c^{SEI}	0.5	X_c[a]	10%
M_{SEI}	0.162 kg/mol	X_c^{ref}[a]	10%
ρ_{SEI}	1690 kg/m^3	$a_c^{ref} i_0^{sol}$[a]	10 A/m^3
k_{Mn_dep}[a]	80×10^{-9} m/s	k_{decom}[a]	7.13×10^{-10} m^6/mol^{2}s
$\alpha_c^{Mn\_dep}$	0.5	$D_{H^+}^{eff}$[a]	$10 \times 10^{-11}\varepsilon_2^p$ m^2/s
λ_{Mn_dep}[a]	3×10^6 1/m	$D_{Mn^{2+}}^{eff}$[a]	$5 \times 10^{-11}\varepsilon_2^p$ m^2/s
k_{H_2}[a]	2.07×10^{-8} m/s	$D_{H_2O}^{eff}$[a]	3×10^{-11} ε_2^p m^2/s
λ_{H_2}[a]	2×10^5 1/m	$\bar{V}$	1.4×10^{-4} m^3/mol
$\alpha_c^{H_2}$	0.5	k_{iso}[a]	8
k_{dis}[a]	2×10^{-9}m/s	k_{res}[a]	3×10^4 Ωm
f_{Mn_dis}[a]	40%		

[a]Assumed values

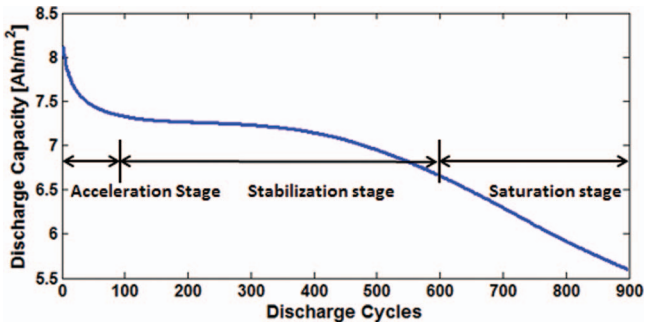

Figure 2. Degradation of discharge capacity after 900 cycles. The degradation is divided to three stages: acceleration stage, stabilization stage and saturation stage.

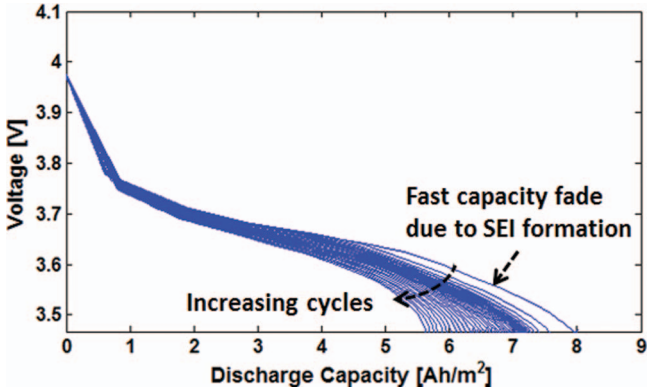

Figure 3. Discharge curves of aged graphite/LMO cell every 20 cycles during 900 cycles. The fast capacity fade is observed at the initial cycles due to the SEI formation induced cyclable lithium loss.

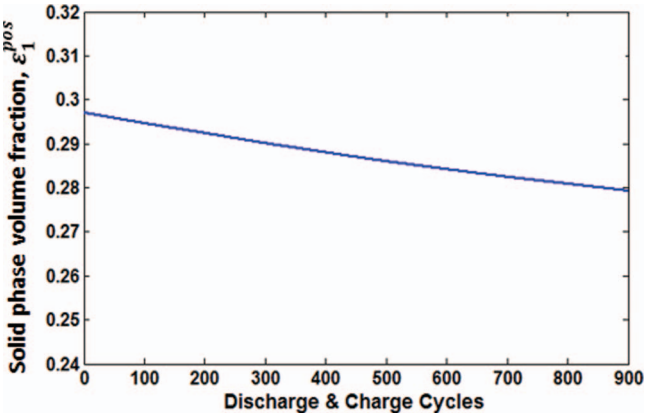

Figure 5. Cathode active material volume fraction change over 900 cycles. The Mn dissolution leads to the cathode active material loss and therefore the volume fraction decreases.

potential curve near the end of discharges is observed; this is due to fast cyclable lithium loss induced by SEI formation in the acceleration stage. As the cycling number increases, the capacity decreases, and the cell voltage reaches the cutoff voltage earlier. The SEI formation induced potential shift was also confirmed in experiments. Amatucci et al.[29] studied the degradation of $LiMn_2O_4$/coke cell and a quick shift of potential was observed. They reported that a surface electrolyte interface layer was formed on the coke surface. This passive layer reduced the cyclable lithium and led to the observed capacity fade and potential shift.

Figures 4 and 5 show cyclable lithium loss and active material loss due to the side reactions, which provide us more insight as to what happens inside the cell.

The main side reactions consuming the cyclable lithium are SEI formation and Mn deposition. Many studies have identified a relationship of SEI growth thickness $\propto t^{1/2}$ and demonstrated that the SEI parabolic growth law fit the experimental data very well.[30] As shown in Fig. 4, the SEI formation curve from our simulation is also consistent with the parabolic growth law. SEI formation contributes to the most significant part of cyclable lithium loss. The Mn deposition-induced cyclable lithium loss is negligible compared to the SEI formation. Therefore, SEI formation dominates cyclable lithium loss during cycling. Figure 4 shows that in initial cycles the SEI layer consumes 7% of the cyclable lithium when the paricles have a radius of 12.5 μm. Smith et al studied the SEI growth by high precision coulometry.[30] They reported about 8% lithium loss after 25 days which is about 250 cycles in our simulation. The lithium loss from our simulation is about 7% after 250 cycles and is very close to their experiment data.

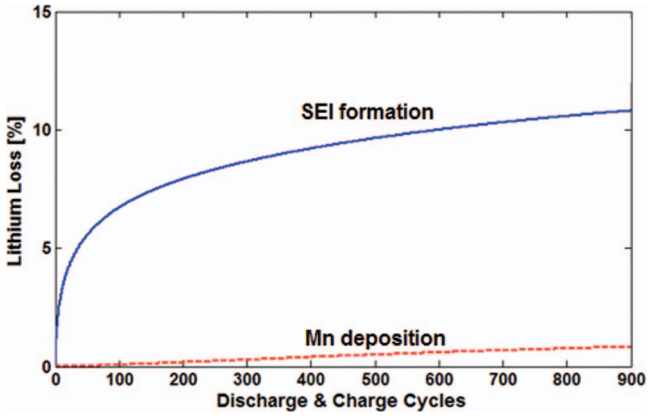

Figure 4. Side reaction induced cyclable lithium loss. SEI formation is the major contributor to cyclable lithium loss, and the loss is fast during initial cycles.

Mn deposition causes additional cyclable lithium loss. The speed of the Mn deposition is stable through the whole cycling life due to the high penetration of Mn^{2+} through the SEI layer and the continuous dissolution of Mn^{2+} from the cathode.

Cyclable lithium loss contributes the most capacity loss in the acceleration stage; the active material loss becomes important when the cell enters the stabilization and saturation stages. Figure 5 presents the change of active material volume fraction during cycling. After 900 cycles the solid phase volume fraction decreases to 0.279, which is about 94% of the initial value. The decrease of the solid phase volume fraction contributes to capacity fade in three ways. First, the Mn dissolution-induced active material loss leads to a decrease of conductivity of the solid phase. Second, the active material loss itself and the induced structure distortion contribute to capacity fade. Third, the active material loss leads to contact loss of the active particle with the conductive network, which causes the isolation of active particles. All together, the decrease of the solid volume fraction will reduce the effective capacity of the cathode electrode.

Capacity fade analysis.— As discussed in the previous sections, there are three stages of Lithium ion battery capacity fade. In order to clearly explore the effects of different degradation mechanisms on the capacity fade and battery performance at each stage, evolutions of the SOC swing windows of each individual electrode are investigated. Particle isolation and loss of active materials are considered in our model. Here we wish to emphasize that the SOC of an electrode as defined earlier accounts for particles still in good contact with the conducting network, and is not an average of all the connected and non-connected particles.

Acceleration stage.— Figure 6 shows the evolution of the SOC swing window on the anode during 900 cycles. In the initial cycles, the anode SOC swing window starts to move down due to the sudden lithium loss. The SEI layer growth during the initial cycles consumes significant amounts of cyclable lithium in the anode, which drags the SOC swing window down in the anode. Due to the mass conservation in the system, the cyclable lithium in the cathode also decreases in the initial cycles as shown in Fig. 7.

The SOC swing window shift on both the anode and cathode affects the voltage response of each electrode. As shown in the bottom of Fig. 6, the lower SOC in the anode increases anode potential, which leads to earlier termination of discharge. The lower SOC swing window also increases cathode potential leading to earlier termination of charge. The shift of the swing windows toward the steep potential side accelates capacity fade. As a result of cyclable lithium loss in the anode, both electrodes are pushed to the high steep voltage region. Further, the high voltage on the cathode also speeds up electrolyte oxidation, thereby accelerating Mn dissolution. In the acceleration stage,

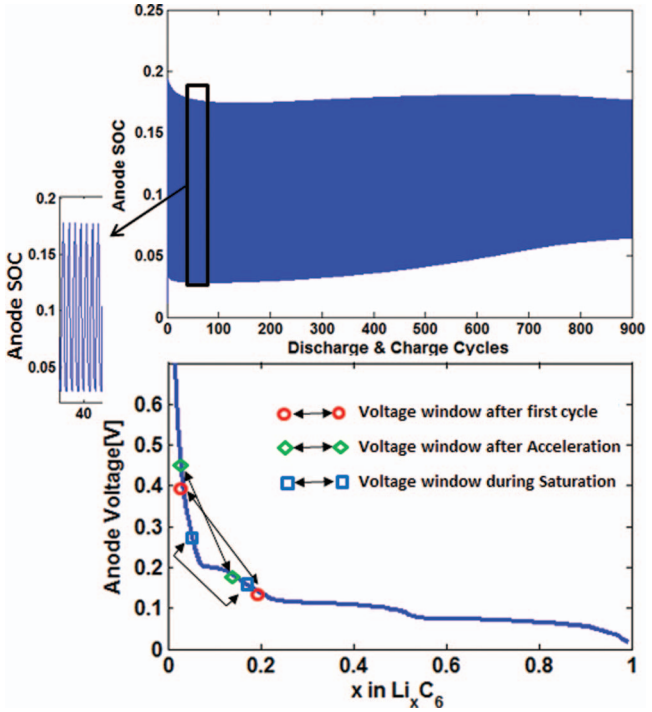

Figure 6. SOC swing window on the anode. Each pair of markers indicate the SOCs at the end of discharge/charge that are representative of different stages. The lower markers correspond to the charged state, the higher markers correspond to the discharged state.

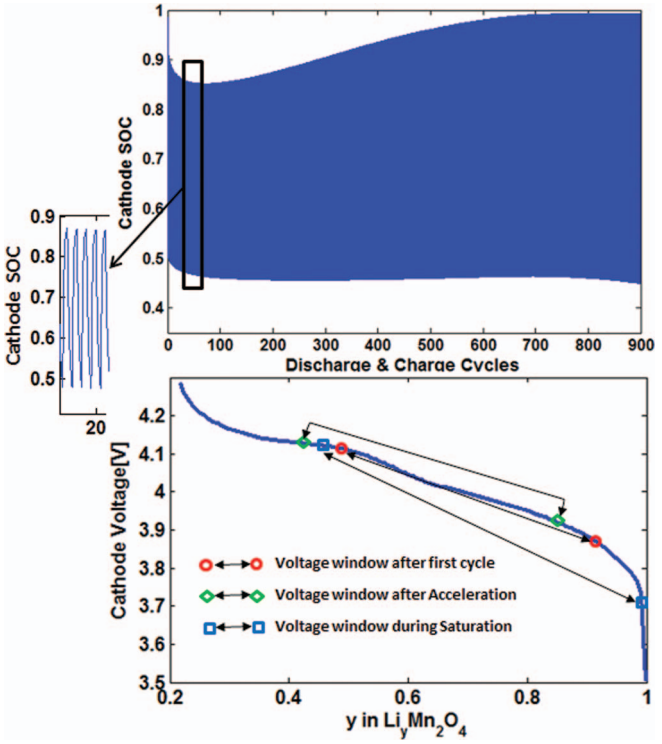

Figure 7. SOC swing window on the cathode. Each pair of markers indicate the SOCs at the end of discharge/charge that are representative of different stages. The lower markers correspond to the discharged state, the higher markers correspond to the charged state.

the side reaction induced cyclable lithium loss dominates capacity fade.

Stabilization stage.— As the SEI layer grows thicker, the SEI formation on the anode surface slows down, and the battery enters the stabilization stage. In this stage the battery performance is relatively stable, and the capacity slowly decreases.

As shown in Figs 6 and 7, the SOC swing windows on both electrodes shift up after entering the stabilization stage. At the same time, the cyclable lithium loss continues at a relatively slow rate compared to the acceleration stage. In the stabilization stage, the active material loss outpaces the loss of cyclable lithium; therefore, SOC on both electrodes are raised up. The shift up of SOC swing windows also brings the electrode voltage back to a relatively flat voltage region. In this stage, because of the low lithium loss rate and low active material loss, the battery works in a relatively balanced way, which benefits cell capacity performance.

Saturation stage.— After the acceleration and stabilization stages, Mn dissolution continues, and dissolution induced active material loss, particle structure distortion and particle isolation develop further. The final result is poor capacity of the cathode. After hundreds of cycles, the capacity of the cathode is insufficient to accommodate all cyclable lithium. Therefore, more and more lithium ions are left in the anode. As shown in Fig. 6, lithium in the anode increases. Due to the small capacity of the cathode, the cathode is almost fully intercalated, even with a small amount of lithium. The poor capacity on the cathode makes the cathode quickly saturated during discharge, and also quickly depleted during charge. As shown in Fig. 7, the SOC swing window on the cathode side becomes wider in the saturation stage due to the small capacity. The anode potential is pushed to a low level due to the increased concentration, and the SOC swing window of anode shrinks due to the small amount of Li interaction and deintercalation.

The three stages of degradation has been observed in experiments. Zhang et al. studied the capacity degradation pattern of lithium ion batteries based on a series of long term cycling data.[5] A parameter estimation technique was used to investigate the parameter trajectories along cycling. Their results showed a clear three stage capacity degradation pattern, which support our model prediction of acceleration, stabilization and saturation stages.

Conclusions

A physics-based electrochemical model is developed to comprehensively study the capacity fade of Li-ion batteries. This model includes the key degradation mechanisms in both anode and cathode materials of the Li-ion battery.

The effects of different degradation mechanisms on capacity fade and battery performance are studied quantitatively. Our study shows that there are three stages during the battery degradation: the acceleration stage, the stabilization stage and the saturation stage. In the acceleration stage, the cyclable lithium loss due to the SEI formation is dominant. When the SEI layer grows thicker and the side reaction rate decays, the degradation enters the stabilization stage. In this stage, the loss of the active material on the cathode outpaces the cyclable lithium loss, and the concentration of both electrodes starts to increase. In the stabilization stage, the lithium ion battery has relatively stable performance. As Mn dissolution continues further, the cathode loses enough capacity to contain all cyclable lithium ions. More and more cyclable lithium is left in the anode, and the total amount of cyclable lithium ions in the system decreases at very low rate. The poor capacity of the cathode makes the cathode quickly saturated during discharge and also quickly depleted during charge, which accelerates capacity fade.

In our study Mn reduction and precipitation at the anode is deemed to affect the cell by reducing the amount of cyclable lithium, much in the same way that SEI film formation at the anode operates. We have assumed that the SEI structure is independent from Mn deposition. However, it is likely that the Mn deposition may fundamentally change

the nature of SEI, such as porosity, ionic conductivity and stability. These coupling effects need more studies and will be considered in our future modeling effort.

In future work we plan to perform a sensitivity analysis with our model to investigate how variation of parameters leads to different dominating degradation mechanisms. The study will look at operational parameters such as discharge profile, environmental parameters such as temperature, and material parameters such as electrode porosity or water concentration in the electrolyte. The study will help to optimize the charge and discharge protocols for extended battery life, and to optimize the power delivery profile to balance performance and battery life in automotive and other applications.

Acknowledgments

This effort was supported by the General Motors/University of Michigan Advanced Battery Coalition for Drivetrains, with additional sponsorship by the Department of Energy. The authors appreciate the support from their sponsors.

List of Inputs

a_s	active surface area per unit electrode volume, 1/m, measured[27]
$c_{1,max}$	maximum solid phase concentration, mol/m^3, measured[27]
c_{EC}	solvent concentration, mol/m^3, measured[4]
D_1	solid phase Li diffusion coefficient, m^2/s, measured[27]
D_2	electrolyte phase Li diffusion coefficient, m^2/s, measured[27]
D_2^{eff}	effective electrolyte phase Li diffusion coefficient, m^2/s, measured[27]
$D_{H^+}^{eff}$	effective diffusivity of H^+, m^2/s, fitted
$D_{Mn^{2+}}^{eff}$	effective diffusivity of Mn^{2+}, m^2/s, fitted
$D_{H_2O}^{eff}$	effective diffusivity of H_2O, m^2/s, fitted
f_{-}^{+}	electrolyte activity coefficient, measured[27]
f_{H^+}	fraction coefficient of proton generation, fitted
f_{Mn_dis}	fraction coefficient for Mn^{2+} dissolution, fitted
F	Faraday constant, C/mol
i_0	exchange current density, A/m^2, measured[27]
k_0	reaction rate coefficient, m/s, measured[27]
k_1	solid phase conductivity, S/m, measured[27]
k_1^{eff}	effective conductivity of solid phase, S/m, measured[27]
k_2	electrolyte phase ionic conductivity, S/m, measured[27]
k_2^{eff}	effective electrolyte phase ionic conductivity, S/m, measured[27]
k_{2D}^{eff}	effective electrolyte phase Li diffusion conductivity, A/m, measured[27]
k_{decom}	reaction coefficient of salt decomposition, m^6/mol^{2}s, fitted
k_{dis}	reaction rate constant for the acid attack on the active material, m/s, fitted
k_{H_2}	reaction rate constant for H_2 generation, m/s, fitted
k_{iso}	particle isolation coefficient, fitted
k_{Mn_dep}	reaction rate constant of Mn deposition, m/s, fitted
k_{res}	SEI resistivity, Ω m, fitted
k_{SEI}	reaction rate constant of SEI, m/s, fitted
M_{SEI}	molecular weight of SEI, kg/mol, measured[4]
p	Bruggeman porosity exponent, measured[27]
R	gas constant, J/(mol K)
R_s	particle radius, m, measured[27]
t_+^0	Li transference number, measured[27]
U_-	negative electrode equilibrium potential, V, measured in our lab
U_+	positive electrode equilibrium potential, V, measured in our lab
U_{oxid}^{eq}	equilibrium potential of solvent oxidation, V, fitted
$\overline{V}$	molar volume of LMO, m^3/mol, measured[12]
X_c	carbon content, measured[12]
X_c^{ref}	carbon content for a preset value, measured[12]
α_a	anodic charge transfer coefficient for lithium intercalation or deintercalation, measured[27]
α_a^{sol}	anodic charge transfer coefficient for solvent oxidation, fitted
α_c	cathodic charge transfer coefficient for lithium intercalation or deintercalation, measured[27]
$\alpha_c^{H_2}$	cathodic charge transfer coefficient for H_2 generation, fitted
$\alpha_c^{Mn\_dep}$	cathodic charge transfer coefficient for Mn deposition, fitted
α_c^{SEI}	cathodic charge transfer coefficient for SEI formation, fitted
ε_1	active material volume fraction, measured[27]
ε_2	electrolyte phase volume fraction, measured[27]
ε_3	polymer and conductive filler volume fraction, measured[27]
λ_{H_2}	limiting coefficient of H_2 generation, 1/ m, fitted
λ_{Mn_dep}	limiting coefficient of Mn deposition, 1/m, fitted
λ_{SEI}	limiting coefficient of SEI reaction, 1/m, fitted
ρ_{SEI}	SEI density, kg/m^3, measured[4]

Appendix

The equilibrium potentials for LMO cathode and graphite anode are obtained by C/50 charge and discharge on a 90:5:5 mass ratio anode half-cell and cathode half-cell, respectively, as shown in Fig. A-1 and Fig. A-2. The electrolyte ionic conductivity is shown in Fig. A-3, which is a function of salt concentration.[27]

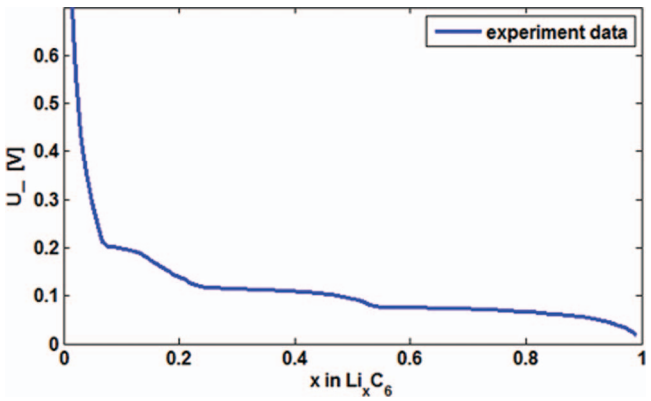

Figure A-1. Equilibrium potential for anode.

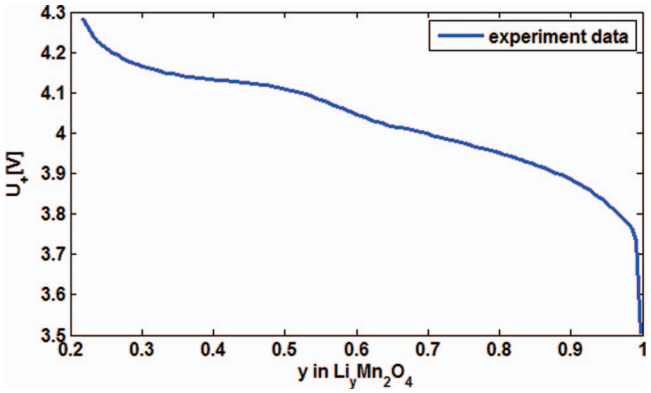

Figure A-2. Equilibrium potential for cathode.

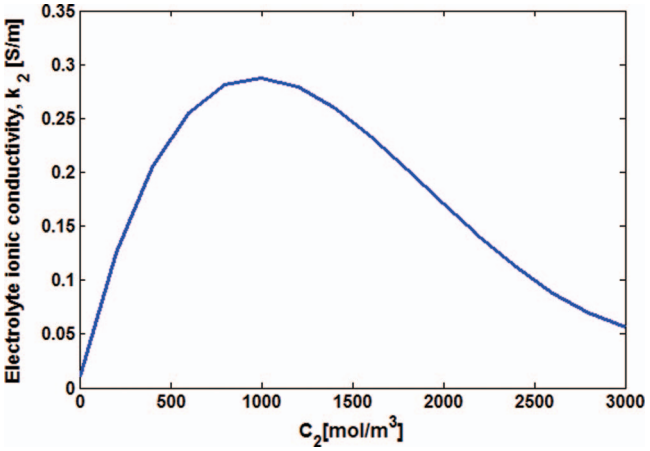

Figure A-3. Electrolyte phase ionic conductivity.

References

1. M. Woon, X. Lin, A. Ivanco, and A. Moskalik, *SAE Technical Paper*, 01 (2011).
2. X. Lin, A. Ivanco, and Z. Filipi, *SAE International Journal of Alternative Powertrains*, **1**, 249 (2012).
3. P. Ramadass, B. Haran, R. White, and B. N. Popov, *J. Power Sources*, **112**, 614 (2002).
4. M. Safari, M. Morcrette, A. Teyssot, and C. Delacourt, *J. Electrochem. Soc.*, **156**, A145 (2009).
5. Q. Zhang and R. E. White, *J. Power Sources*, **179**, 793 (2008).
6. P. Arora, R. E. White, and M. Doyle, *J. Electrochem. Soc.*, **145**, 3647 (1998).
7. R. Fong, U. von Sacken, and J. R. Dahn, *J. Electrochem. Soc.*, **137**, 2009 (1990).
8. D. H. Jang, Y. J. Shin, and S. M. Oh, *J. Electrochem. Soc.*, **143**, 2204 (1996).
9. D. H. Jang and S. M. Oh, *J. Electrochem. Soc.*, **144**, 3342 (1997).
10. J. Park, J. H. Seo, G. Plett, W. Lu, and A. M. Sastry, *Electrochem. Solid-State Lett.*, **14**, A14 (2011).
11. C.-H. Lu and S.-W. Lin, *J. Mater. Res.*, **17**, 1476 (2002).
12. Y. Dai, L. Cai, and R. E. White, *J. Electrochem. Soc.*, **160**, A182 (2013).
13. Y. Xia, Y. Zhou, and M. Yoshio, *J. Electrochem. Soc.*, **144**, 2593 (1997).
14. S. Komaba, B. Kaplan, T. Ohtsuka, Y. Kataoka, N. Kumagai, and H. Groult, *J. Power Sources*, **119**, 378 (2003).
15. K. Smith and C.-Y. Wang, *J. Power Sources*, **161**, 628 (2006).
16. S. Komaba, N. Kumagai, and Y. Kataoka, *Electrochim. Acta*, **47**, 1229 (2002).
17. A. M. Colclasure, K. A. Smith, and R. J. Kee, *Electrochim. Acta*, **58**, 33 (2011).
18. M. McArthur, S. Trussler, and J. Dahn, *J. Electrochem. Soc.*, **159**, A198 (2012).
19. D. Aurbach, Y. Ein-Eli, O. Chusid, Y. Carmeli, M. Babai, and H. Yamin, *J. Electrochem. Soc.*, **141**, 603 (1994).
20. A. Blyr, C. Sigala, G. Amatucci, D. Guyomard, Y. Chabre, and J. M. Tarascon, *J. Electrochem. Soc.*, **145**, 194 (1998).
21. J. Choa and M. M. Thackeray, *J. Electrochem. Soc.*, **146**, 3577 (1999).
22. N.-S. Choi, J.-T. Yeon, Y.-W. Lee, J.-G. Han, K. T. Lee, and S.-S. Kim, *Solid State Ionics*, **219**, 41 (2012).
23. T. Kawamura, S. Okada, and J.-i. Yamaki, *J. Power Sources*, **156**, 547 (2006).
24. E. Wang, D. Ofer, W. Bowden, N. Iltchev, R. Moses, and K. Brandt, *J. Electrochem. Soc.*, **147**, 4023 (2000).
25. D. Guyomard and J. M. Tarascon, *J. Electrochem. Soc.*, **140**, 3071 (1993).
26. M. Kerlau, J. A. Reimer, and E. J. Cairns, *Electrochem. Commun.*, **7**, 1249 (2005).
27. M. Doyle, J. Newman, A. S. Gozdz, C. N. Schmutz, and J. M. Tarascon, *J. Electrochem. Soc.*, **143**, 1890 (1996).
28. R. Spotnitz, *J. Power Sources*, **113**, 72 (2003).
29. G. G. Amatucci, N. Pereira, T. Zheng, and J.-M. Tarascon, *J. Electrochem. Soc.*, **148**, A171 (2001).
30. A. Smith, J. C. Burns, X. Zhao, D. Xiong, and J. Dahn, *J. Electrochem. Soc.*, **158**, A447 (2011).